

A THEORETICAL MODEL FOR CARDIAC MECHANICS: EFFECTS OF
INTERVENTRICULAR INTERACTIONS

by

Vivian Tuong Nguyen

Copyright © Vivian Nguyen 2024

A Thesis Submitted to the Faculty of the

DEPARTMENT OF BIOMEDICAL ENGINEERING

In Partial Fulfillment of the Requirements

For the Degree of

MASTER OF SCIENCE

In the Graduate College

THE UNIVERSITY OF ARIZONA

2024

THE UNIVERSITY OF ARIZONA
GRADUATE COLLEGE

As members of the Master's Committee, we certify that we have read the thesis prepared by *Vivian Nguyen*, titled *A theoretical model for cardiac mechanics: effects of interventricular interactions* and recommend that it be accepted as fulfilling the dissertation requirement for the Master's Degree.



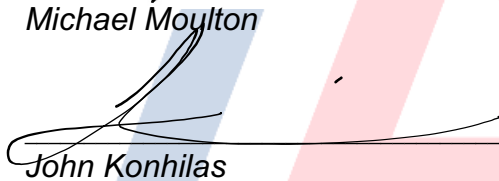
Timothy Secomb

Date: 5/10/2024



Michael Moulton

Date: 5/10/2024



John Konhilas

Date: 5/10/2024

Final approval and acceptance of this thesis is contingent upon the candidate's submission of the final copies of the thesis to the Graduate College.

I hereby certify that I have read this thesis prepared under my direction and recommend that it be accepted as fulfilling the Master's requirement.



Timothy Secomb
Master's Thesis Committee Chair
Department of Physiology

Date: 5/10/2024

Contents

1 Abstract	5
2 Introduction	6
3 Methods	8
3.1 Spatially resolved LV and RV model	8
3.2 Aorta, valve, and circulation model	13
4 Results	17
4.1 Normal cardiac function	17
4.2 Cardiac function with pulmonary hypertension	18
4.3 Effects of interventricular interaction	20
5 Discussion	21
6 References	23

List of Figures

1	LV axisymmetric initial configuration of prolate spheroidal shell.	9
2	Non-axisymmetric biventricular shape.	9
3	Schematic of coordinate spaces and transformations.	10
4	Visualization of reference to axisymmetric coordinate pull-back.	14
5	Schematic of circulatory system model depicted as an electrical circuit. . .	16
6	Long-axis and short-axis views of LV and RV wall deformations during the cardiac cycle.	17
7	Normal pressure-volume loops: LV and RV.	18
8	Normal pressures: LV, RV, aorta, and pulmonary arteries.	18
9	Normal flow rates through the tricuspid, pulmonary, mitral, and aortic valves.	18
10	LV PV loops: Normal; Five times pulmonary resistance and RV contractility.	19
11	RV PV loops: Normal; Five times pulmonary resistance and RV contractility.	19
12	Mitral valve flow rate: Normal; Five times pulmonary resistance and contractility.	19
13	Short-axis view of LV and RV showing septal displacement when interventricular interactions are included and no shift when excluded.	20
14	Decrease in LV stroke volume in response to increased pulmonary resistance and RV contractility.	20
15	Decrease in LV systolic pressure in response to increased pulmonary resistance and RV contractility.	20

1 Abstract

The left and right ventricles (LV, RV) of the heart are mechanically linked by the interventricular septum. Changes in volume, pressure and contractility of one ventricle can affect the other by shift and deformation of the septum. This coupling of the systolic and diastolic functions between the ventricles is known as interventricular interactions. Studying the role of ventricular dependence is relevant in several cardiomyopathies including atrial septal defects, mitral stenosis, cor pulmonale, RV failure after implantation of LV assist device, and pulmonary hypertension. In this work, we present a spatially-resolved, biventricular model of the heart that can be used to investigate the effects of septal displacement and LV-RV interactions in the context of pulmonary hypertension and to quantify its effects on local and global hemodynamics. The model builds from a low-order, computationally efficient model of a prolate spheroidal, axisymmetric LV connected in series to a closed circulation and is adapted to allow for non-axisymmetric deformations, including the introduction of the RV cavity as an appendage to the LV. By using this representation of the complex geometry of both the LV and RV, model parameters can be matched to fit individualized patient geometries from echocardiogram data. Simulations of cardiac cycles in response to acute increases to pulmonary resistance suggest that the heart can only function with increased pulmonary resistance if there is RV hypertrophy. To represent the effects of RV hypertrophy, the force of RV contractility is increased in proportion to increases in pulmonary resistance. According to the model, increasing pulmonary resistance and RV contractility leads to a large increase in pulmonary artery pressure, but systemic arterial pressure and stroke volume show significant decreases. The inclusion of interventricular interaction had little effect on stroke volume response, but significantly dampened the reduction in LV pressure with decreased preload. The model suggests that increased RV contractility with septal displacement helps maintain LV pressure in pulmonary hypertension. This biventricular model is suited for quantifying the role of interventricular interactions in pulmonary hypertension and can be applied to various cardiomyopathies.

2 Introduction

The interaction between the left and right ventricle, referred to as **ventricular interdependence**, is a significant determinant of cardiac function. The ventricles are separated by the interventricular septum and share common myocardial fibers. Therefore, any functional or structural change in one ventricle, such as hypertrophy or dilation caused by pressure overload, can affect the pressure-volume relationship in the other ventricle. Left ventricular (LV) force generation is required for the development of sufficient right ventricular pressures during systole, and changes in right ventricular (RV) volume can affect pressures developed in the left ventricle. Such effects are referred to as **systolic ventricular interdependence** [1, 2]. During diastole, volume overload of either ventricle shifts the interventricular septum, decreasing the compliance and compressing the other ventricle, resulting in **diastolic ventricular interdependence** [2]. Any of these effects can result in impaired circulatory function. For example, during systole, impaired LV contractility can affect RV function. During diastole, RV volume overload due to pulmonary hypertension can impede filling of the LV and has been implicated as one possible mechanism of heart failure with preserved ejection fraction (HFpEF). However, diagnosis and treatment of pulmonary hypertension and HFpEF is challenging because symptoms are masked behind sustained LV systolic function. The effects of ventricular interaction can be significant in both HFpEF and heart failure with reduced ejection fraction (HFrEF) and have therefore been studied extensively in animal models [2, 3, 4, 5] and in patients [6, 7, 8, 9]. However, none of these studies have been able to isolate the hemodynamic effects of direct interventricular interactions [10]. Experimental study of interventricular interaction generally requires invasive hemodynamic measurements including biventricular catheterization. Such measurements require significant risks and are generally not possible in human patients for diagnosis in routine diagnosis and screening.

Theoretical modeling provides a means to investigate the effects of interventricular dynamics on cardiac function in normal and diseased states, because it can describe the complex interactions among the chambers of the heart and throughout the circulatory system. Recent advancements in doppler echocardiography have also allowed clinicians to acquire detailed information on patient specific heart geometries and local hemodynamics (i.e. pressures and flows) with high temporal resolution. Together with echocardiographic imaging, theoretical modeling has the potential to guide improved patient-specific diagnosis and interventional planning [11].

Several approaches to modeling interventricular interactions have been explored. Time-varying elastance models represent the pressure-volume relationship between the heart chambers as a function of elastance varying over a cardiac cycle [12]. However, such lumped parameter models lack an explicit representation of the heart geometry and measure all deformations of the heart in terms of volume change. In addition, the finite element method can be used to resolve a highly detailed description of cardiac deformation by computing and summing over local displacement variations [13]. Although these models are used in many applications, such analyses are computationally rigorous as many degrees of freedom are required to describe local element displacements. Generating

a single cardiac cycle can take several hours which renders FEM models impractical for routine clinical use.

A model that can be used to guide diagnosis and treatment planning must be computationally fast to allow for investigation of a range of conditions and assumptions. Model parameters must be easily approximated to fit individualized patient geometries. Additionally, investigating the effects of ventricular interdependence on cardiac function requires an explicit representation of the septum to spatially resolve how the ventricles interact. A full closed-loop model is needed to measure interaction between the heart and the circulatory system and represent the entire cardiac cycle. Altogether, we are aiming for an intermediate between minimal lumped parameter models and detailed finite element models that captures the main geometrical features of cardiac mechanics without slowing computation time.

Current approaches include the three-segment (TriSeg) biventricular model developed by Lumens et al. 2009 [14] which represents the LV and RV as overlapping spheres with an explicit septal wall. This model has been used to study ventricular interactions [15], however the spherical approximation of the ventricles does not allow for adaption to individualized geometries which limits its use for patient-specific applications. We seek to develop a model that can leverage available data from Doppler echocardiography to set model parameters and runs fast enough to be used routinely in the clinic.

Models by Moulton and Secomb [16, 17, 18, 19] represent the LV in an idealized prolate-spheroidal geometry and uses only three parameters to capture the main modes of deformation of the LV, including base-to-apex lengthening/shortening, circumferential contraction, and torsion. The other chambers of the heart are represented separately as spheres and are connected via systemic and pulmonary circulation. Although this approach was able to study pathologies related to LV remodeling and loss of contractility, the model fails to represent the physical interaction between the LV and RV via the shared septal wall. Here, we present an extension to the Moulton and Secomb 2023 model [16] that includes LV and RV within a single geometrical construct. Starting from an axisymmetric LV model, the right wall of the LV is split into two components, forming the interventricular septum and the RV free wall. By modeling the RV as an appendage of the LV, we form the characteristic crescent shape of the RV and the septum forms a boundary between both ventricles. By directly attaching the ventricles we can physically model the affects of septal shift and interventricular interactions. Two additional modes of deformation are used to describe the motion of the RV free wall and the septum. For simplicity, the RV is assumed to have the same torsion and fiber characteristics as the left ventricle. This assumption is justified because the RV has a thinner wall, so it likely follows the dominant LV motion. The model is used to analyze the effects of ventricular interaction on cardiac function in conditions of the normal heart and pulmonary hypertension.

3 Methods

3.1 Spatially resolved LV and RV model

Following the model framework established by Moulton and Secomb 2023 [16], the LV reference, or initial, configuration is described as an axisymmetric prolate spheroid shell and prolate spheroidal coordinates (μ, ν, ϕ) are used. The coordinate transformation from Cartesian (x, y, z) coordinates is

$$\begin{aligned} x &= a \sinh \mu \sin \nu \cos \phi \\ y &= a \sinh \mu \sin \nu \sin \phi \\ z &= a \cosh \mu \cos \nu \end{aligned} \quad (1)$$

where $2a$ is the distance between the foci of the prolate spheroid (Figure 1). The Jacobian gives the local linear approximation of the coordinate transformation

$$\begin{aligned} \mathbf{J} &= \begin{bmatrix} \partial x / \partial \mu & \partial x / \partial \nu & \partial x / \partial \phi \\ \partial y / \partial \mu & \partial y / \partial \nu & \partial y / \partial \phi \\ \partial z / \partial \mu & \partial z / \partial \nu & \partial z / \partial \phi \end{bmatrix} \\ &= \begin{bmatrix} a \cosh \mu \sin \nu \cos \phi & a \sinh \mu \cos \nu \cos \phi & -a \sinh \mu \sin \nu \sin \phi \\ a \cosh \mu \sin \nu \sin \phi & a \sinh \mu \cos \nu \sin \phi & a \sinh \mu \sin \nu \cos \phi \\ a \sinh \mu \cos \nu & -a \cosh \mu \sin \nu & 0 \end{bmatrix} \end{aligned} \quad (2)$$

with scale factors $g_\mu = g_\nu = a\sqrt{\sinh^2 \mu + \sin^2 \nu}$ and $g_\phi = a \sinh \mu \sin \nu$. Since prolate spheroid coordinates are orthogonal, the determinant of the Jacobian can be expressed as a product of the scale factors

$$|\mathbf{J}| = g_\mu g_\nu g_\phi = a^3 \sinh \mu \sin \nu (\sinh^2 \mu + \sin^2 \nu) \quad (3)$$

The initial LV cavity size and shape are described by parameters α_0 , the base-to-apex length, and $\mu_{in0}(\nu_0, \phi_0)$, the boundary of the inner wall. The outer wall is defined by $\mu_{out0}(\nu_0, \phi_0)$, which establishes LV thickness, and an imaginary midwall, μ_{mid0} , will diverge into μ_{mid0in} and $\mu_{mid0out}$ between angles $\phi_s < \phi_0 < 2\pi - \phi_s$ to form a crescent shaped RV as an appendage to the LV. Thereby, the midwall μ_{mid0in} forms the outer wall of the septum and $\mu_{mid0out}$ forms the RV inner wall (Figure 2).

We define three configurations to describe the addition of an RV to the axisymmetric LV to the 2023 model and the deformation of the LV, RV, and septal wall. (1) An **axisymmetric LV configuration** with a collapsed RV, coordinates (μ_0, ν_0, ϕ_0) , and $a = a_0$, (2) a non-axisymmetric **unstressed, reference configuration** including the RV with coordinates $(\mu_{ref}, \nu_{ref}, \phi_{ref})$, and (3) a non-axisymmetric time-dependent **deformed configuration** including the RV with coordinates (μ, ν, ϕ) .

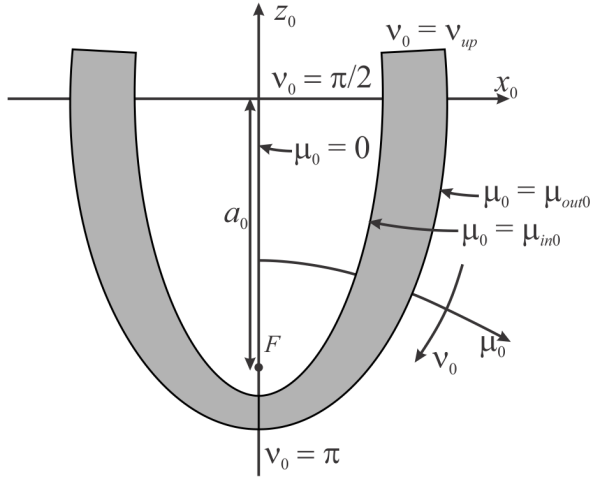


Figure 1: LV axisymmetric initial configuration of prolate spheroidal shell.

Prolate spheroidal coordinates (μ, ν, ϕ) are used to describe the shape of the LV and are shown in with respect to Cartesian coordinates (x, y, z) . The initial configuration is defined by parameter a_0 , where $2a_0$ is the interfocal distance of the prolate spheroid. The thickness of the LV myocardial wall is set by $\mu_{in0} \leq \mu_0 \leq \mu_{out0}$. The LV region is described by the polar angle range $\nu_{up} \leq \nu_0 \leq \pi$ and $-\phi_s \leq \phi_0 \leq \phi_s$, the azimuthal angular region. In the axisymmetric configuration as seen in Moulton et al. 2023 [16], the LV covers an entire circle, i.e. $\phi_s = \pi$.

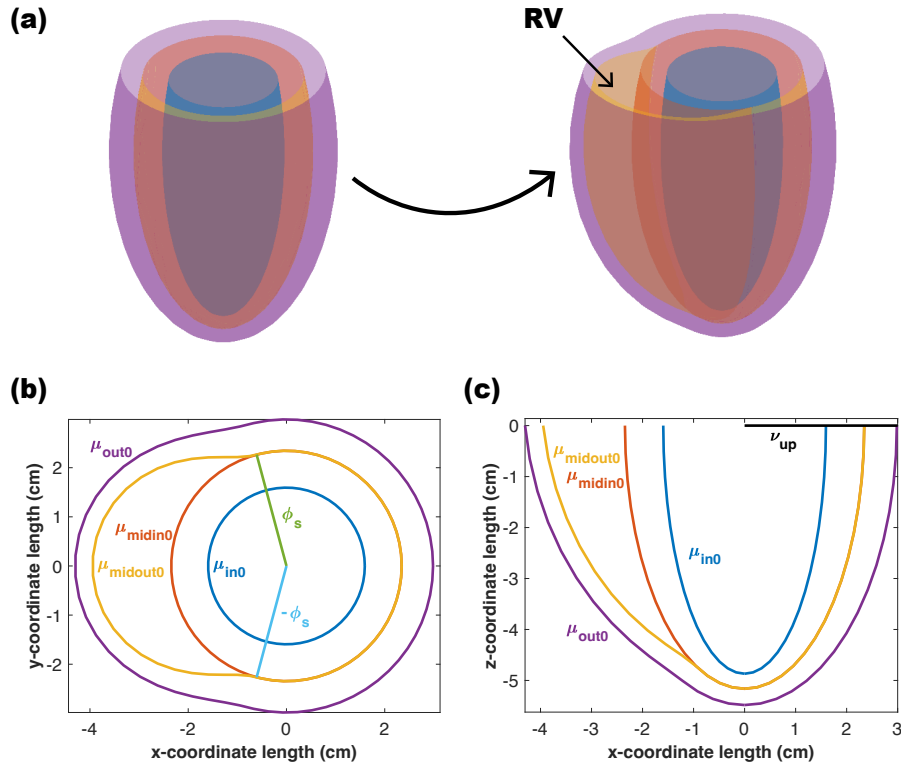


Figure 2: Non-axisymmetric biventricular shape.

(a) Addition of RV to axisymmetric LV (b) Short-axis view of LV and RV with μ_{in0} (blue), μ_{out0} (purple), and μ_{mid} , branching into μ_{midin0} (orange) and $\mu_{midout0}$ (yellow). Branching angle ϕ_s (green) and $-\phi_s$ (light blue), where divergence occurs indicated (c) Long-axis view with same boundaries indicated. Upper boundary of the ventricle, ν_{up} also indicated (black).

The main modes of deformations of the LV and RV are described by families of mappings from the axisymmetric configuration to the reference and deformed configurations as $(a_0; \mu_0, \nu_0, \phi_0) \rightarrow (a; \mu, \nu, \phi)$, where the deformed variables μ , ν , and ϕ are functions of the axisymmetric, unstressed coordinates μ_0, ν_0, ϕ_0 (Figure 3).

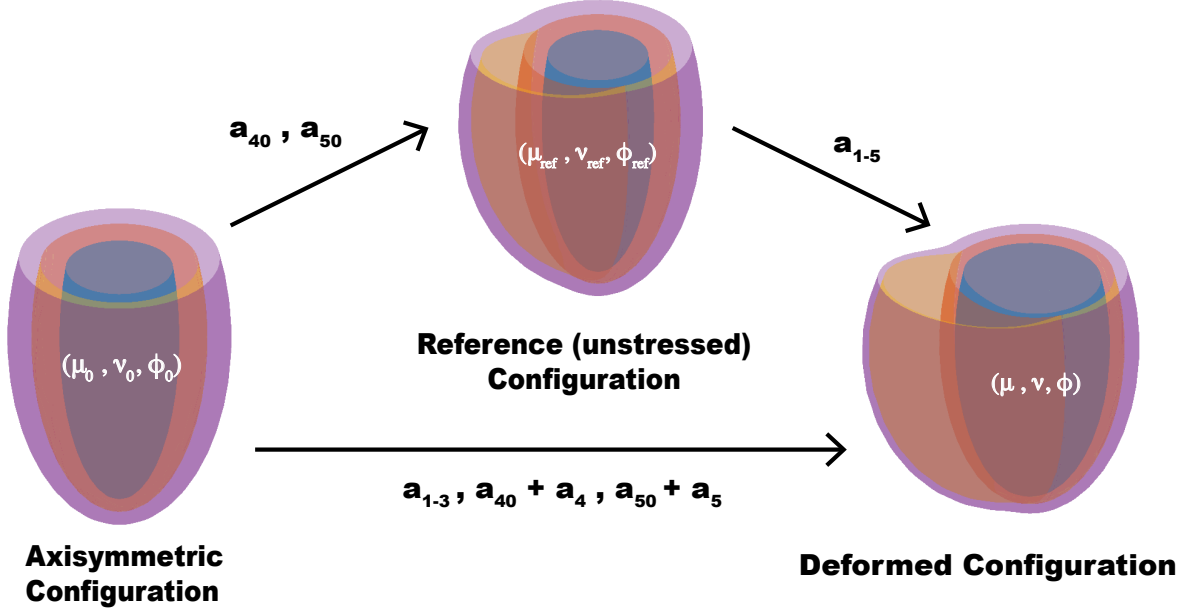


Figure 3: Schematic of coordinate spaces and transformations.

The initial, axisymmetric LV configuration is expressed in μ_0, ν_0, ϕ_0 coordinates. Parameters a_{40} and a_{50} displace the RV free wall and septum in the reference, unstressed configuration $(\mu_{\text{ref}}, \nu_{\text{ref}}, \phi_{\text{ref}})$ and introduces the RV. Time-dependent parameters $a_{1-5}(t)$ deform the ventricles to represent deformation of the heart during the cardiac cycle in μ, ν, ϕ coordinates.

We reduce computation time by limiting deformations with the assumption that the myocardial wall is incompressible, which is a reasonable approximation [18]. The incompressibility condition guarantees volume-preserving wall deformations such that the local volume elements are equal in the axisymmetric initial configuration and the deformed LV and RV configuration:

$$|\mathbf{J}|d\mu d\nu d\phi = |\mathbf{J}_0|d\mu_0 d\nu_0 d\phi_0 \quad (4)$$

Additionally, we also assume that wall deformations occur along lines of constant ν ,

$$\nu = \nu_0 \quad , \quad \frac{\partial \nu}{\partial \nu_0} = 1 \quad (5)$$

and to account for torsion, at a given ν , rotation occurs over a fixed angle ϕ such that

$$\frac{\partial \phi}{\partial \phi_0} = 1 \quad (6)$$

Imposing these kinematic constraints greatly simplifies calculations and still allows for a large family of deformations. Applying conditions (5) and (6), the volume conservation equation (4) reduces to

$$\frac{a^3 \sinh \mu \sin \nu (\sinh^2 \mu + \sin^2 \nu_0)}{a_0^3 \sinh \mu_0 \sin \nu_0 (\sinh^2 \mu_0 + \sin^2 \nu_0)} \frac{\partial \mu}{\partial \mu_0} = 1 \quad (7)$$

Integrating in terms of μ_0 derives an implicit map between μ and μ_0

$$\begin{aligned} a^3 [\cosh \mu (\frac{1}{3} \cosh^2 \mu - \cos^2 \nu) - (\frac{1}{3} - \cos^2 \nu_0)] \\ = a_0^3 [\cosh \mu_0 (\frac{1}{3} \cosh^2 \mu_0 - \cos^2 \nu_0) - (\frac{1}{3} - \cos^2 \nu_0)] + F_0(\mu_0, \nu_0, \phi_0) \end{aligned} \quad (8)$$

To satisfy volume conservation, $\partial F_0 / \partial \mu_0 = 0$ within the tissue domain, while F_0 has an arbitrary dependence on ν_0 and ϕ_0 . This mapping equation can be solved algebraically for $\cosh \mu$. The main modes of deformation of the LV are captured by only three kinematic parameters, $a_{1-3}(t)$. The first parameter a_1 describes lengthening and shortening of the base-to-apex length at constant volume where $a_1 = a - a_0$. Second, a_2 represents circumferential contraction or expansion of the LV and is incorporated into the arbitrary function $F_0 = f(\nu_0)$ over the LV range $-\phi_s \leq \phi_0 \leq \phi_s$. $f(\nu_0)$ is defined to displace the endocardial wall $\mu_{in0} \rightarrow \mu_{in}$ as a function of ν_0 so that the LV cavity volume approaches zero as $a_2 \rightarrow a_0$, representing full ejection.

$$f(\nu_0) = -a_2 a_0^2 [\cosh \mu_{in0} (\frac{1}{3} \cosh^2 \mu_{in0} - \cos^2 \nu_0) + (\frac{1}{3} - \cos^2 \nu_0)] \quad (9)$$

And finally, a_3 produces torsional deformation by a displacement in ϕ along lines of constant $\nu = \nu_0$ from base-to-apex

$$\phi = \phi_0 + a_3 (\cos \nu_0 - \cos \nu_{up}) \quad (10)$$

where torsion is clockwise if $a_3 < 0$, and counterclockwise if $a_3 > 0$ as viewed from the apex.

The major advancement from the Moulton and Secomb 2023 model [16] is the addition of the right ventricle from the axisymmetric LV geometry. We do this by adding a dependence of F_0 on μ_0 as a step discontinuity at $\mu_0 = \mu_{mid0}$ such that $\partial F_0 / \partial \mu_0 = 0$ is still satisfied. This step discontinuity, $h(\mu_0)$, divides μ_{mid0} into an inner boundary, μ_{mid0in} , forming the septum, and an outer boundary, $\mu_{mid0out}$, forming the RV free wall. The RV cavity size is determined by how far apart μ_{mid0in} is from $\mu_{mid0out}$. The time constant parameters a_{40} and a_{50} in the step function, $h(\mu_0)$, deforms the initial axisymmetric LV configuration to the non-axisymmetric LV and RV reference (unstressed) configuration by separating the RV free wall (with a_{40}) and septum (with a_{50}) from an axisymmetric LV wall.

The discontinuity is also sine squared functions of ν_0 and ϕ_0 so that the bifurcation approaches zero smoothly at the edges of the RV region and has continuous first derivatives for stable stress calculations. Therefore, we extend our definition of F_0 in the RV

$$F_0(\mu_0, \nu_0, \phi_0) = f(\nu_0) + h(\mu_0)j(\nu_0)g(\phi_0) \quad (11)$$

where

$$h(\mu_0) = \begin{cases} a_{50} + a_5 & \text{if } \mu_{in0} \leq \mu_0 < \mu_{mid0} \\ a_{40} + a_4 & \text{if } \mu_{mid0} < \mu_0 \leq \mu_{out0} \end{cases} \quad (12)$$

$$j(\nu_0) = \begin{cases} \sin^2(\alpha\nu_0) & \text{if } \alpha\nu_0 \leq \pi \\ 0 & \text{if } \alpha\nu_0 > \pi \end{cases} \quad (13)$$

$$g(\phi_0) = \begin{cases} 0 & \text{if } -\phi_s \leq \phi_0 < \phi_s \\ \sin^2\left(\frac{6}{5}(\phi_0 - \phi_s)\right) & \text{if } \phi_s \leq \phi_0 \leq 2\pi - \phi_s \end{cases} \quad (14)$$

The angular LV region is defined as $-\phi_s \leq \phi_0 < \phi_s$ and the RV region is $\phi_s \leq \phi_0 \leq 2\pi - \phi_s$. The constant α in $j(\nu_0)$ is chosen to set the position of the bifurcation from the apical end of the RV from the apex of the LV. The deformation of the RV is described by two additional kinematic parameters a_4 and a_5 , which further displace the RV free wall and septum respectively in response to stress. In the reference (unstressed) configuration, parameters $a_4 = a_5 = 0$. Together, parameters $a_{1-5}(t)$ describe the modes of deformation of the LV and RV in the deformed configuration as summarized in Table 1.

Table 1: Time-dependent parameters describing LV and RV dynamics

Kinematic Parameter	Mode of deformation
a_1	LV base-to-apex lengthening and shortening
a_2	LV volume conserving circumferential contraction and expansion
a_3	LV and RV torsion
a_4	RV free wall displacement
a_5	Septum wall displacement

The deformation gradient tensor, \mathbf{F} , describes locally the transformation from the initial LV axisymmetric configuration to the LV and added RV deformed state. \mathbf{F} is found by taking the derivatives of the prolate spheroidal deformed coordinates $i = \mu, \nu, \phi$ with respect to the initial coordinates $j = \mu_0, \nu_0, \phi_0$

$$F_{ij} = \begin{bmatrix} F_{\mu\mu_0} & F_{\mu\nu_0} & F_{\mu\phi_0} \\ 0 & F_{\nu\nu_0} & 0 \\ 0 & F_{\nu\nu_0} & F_{\phi\phi_0} \end{bmatrix} = \begin{bmatrix} \frac{g_\mu}{g_{\mu_0}} \frac{\partial \mu}{\partial \mu_0} & \frac{g_\mu}{g_{\nu_0}} \frac{\partial \mu}{\partial \nu_0} & \frac{g_\mu}{g_{\phi_0}} \frac{\partial \mu}{\partial \phi_0} \\ 0 & \frac{g_\nu}{g_{\nu_0}} \frac{\partial \nu}{\partial \nu_0} & 0 \\ 0 & \frac{g_\phi}{g_{\nu_0}} \frac{\partial \phi}{\partial \nu_0} & \frac{g_\phi}{g_{\phi_0}} \frac{\partial \phi}{\partial \phi_0} \end{bmatrix} \quad (15)$$

Calculating the deformation gradient tensor components verify that the incompressibility condition, $\det(\mathbf{F}) = F_{\mu\mu_0} F_{\nu\nu_0} F_{\phi\phi_0} = 1$, is satisfied, ensuring that only volume-conserving deformations are made. The Green-Lagrange strain tensor is given by $\mathbf{E} = \frac{1}{2}(\mathbf{F}^\top \mathbf{F} - \mathbf{I})$ and the second Piola-Kirchoff (PK2) stress is given by $\mathbf{S} = \mathbf{J} \mathbf{F}^{-1} \mathbf{F}^{-\top}$. For hyperelastic material as with the myocardium, the Green strain and PK2 stress are related by strain energy function Ψ , which describes the stored energy per volume of deformed tissue

$$S_{ij} = \partial \Psi / \partial E_{ij} \quad (16)$$

where $\partial \Psi$ is the work done over an incremental deformation. Integrating equation (16) over the volume of myocardial tissue, V , with respect to each deformation parameter

$a_n = a_{1-5}$ yields an equation for virtual work of the system associated with a change in parameter

$$\iiint_V \frac{\partial \mathbf{E}}{\partial a_n} : \mathbf{S} dV \quad (17)$$

By assuming the total virtual work done by an incremental change of each parameter is equal to zero, we solve for the minimum energy equilibrium states of the myocardium as a function of the kinematic parameters. Thus, integrating equation (17) produces a system of nonlinear ordinary differential equations for $a_n(t)$.

The kinematic parameters $a_n(t)$ are applied to displace the LV RV reference configuration to the deformed state. However, we wish to evaluate this integral over the axisymmetric configuration because the boundary of integration is rectangular and not time dependent in axisymmetric domain. One approach would be to establish a rectangular grid in the axisymmetric configuration, map this grid to the reference configuration, then evaluate the integral in the reference coordinates. However, instead we use a simpler method, where we first describe the deformation gradient tensor as a deformation from the axisymmetric configuration to the deformed configuration (Equation 15). We are able to do this because \mathbf{F} , the deformation gradient tensor from the unstressed reference state to the deformed state is equivalent to

$$\mathbf{F} = \mathbf{F}_1 \mathbf{F}_0^{-1} \quad (18)$$

where the deformation gradient tensor \mathbf{F}_1 relates the axisymmetric to the deformed state and \mathbf{F}_0 maps axisymmetric to the reference configuration (Figure 4). Although \mathbf{F} is expressed in terms of the reference coordinates, the covariant pull-back of the Green strain tensor, \mathbf{E} , and contravariant pull-back of the PK2 stress tensor, \mathbf{S} , maps their components in the reference configuration back to the axisymmetric configuration and allows us to express these terms in axisymmetric coordinates

$$\mathbf{E}_0 = \mathbf{F}_0^\top \mathbf{E} \mathbf{F}_0 \quad (19)$$

$$= \frac{1}{2} (\mathbf{F}_1^\top \mathbf{F}_1 - \mathbf{F}_0^\top \mathbf{F}_0)$$

$$\mathbf{S}_0 = \mathbf{F}_0^{-1} \mathbf{S} \mathbf{F}_0^{-\top} \quad (20)$$

Since \mathbf{F}_0 is independent of $a_n(t)$, the pullback of $\partial \mathbf{E}/a_n$ is further simplified to $\partial \mathbf{E}_1/a_n$, with $\mathbf{E}_1 = \frac{1}{2} (\mathbf{F}_1^\top \mathbf{F}_1)$. Thus, virtual work can be integrated over the axisymmetric domain

$$\iiint_{Ref} \frac{\partial \mathbf{E}}{\partial a_n} : \mathbf{S} dV = \iiint_{Axis} \frac{\partial \mathbf{E}_1}{\partial a_n} : \mathbf{S}_0 dV \quad (21)$$

3.2 Aorta, valve, and circulation model

The two atria are represented by thick-walled spheres, whose radii change with respect to volume-preserving wall deformations described by parameters $a_{4-6}(t)$. In all

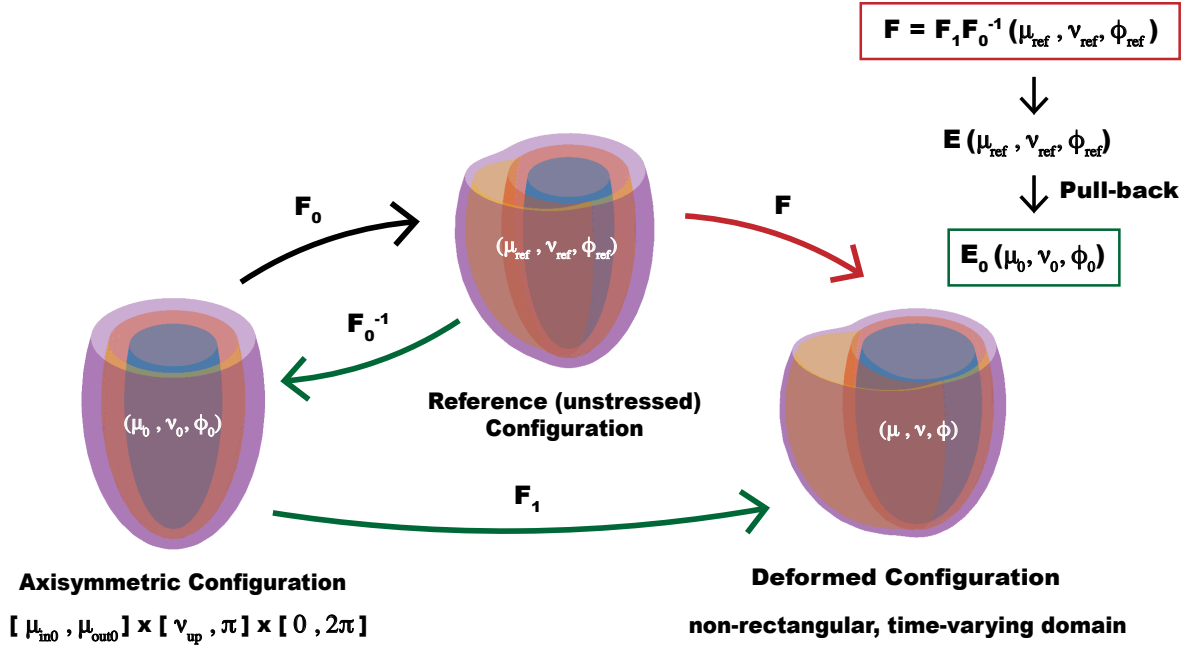


Figure 4: Visualization of reference to axisymmetric coordinate pull-back.

chambers, fiber stresses varies with time according to an activation function, with sarcomere length dependent on the length-tension relationship of cardiac muscle, force-velocity relationship is represented by including a viscous resistance to shortening. We assume viscoelastic passive properties of the myocardium.

The four chambers are connected by a 0-D Bernoulli valve model [20, 21], which represents flow through each valve by the equation

$$L \frac{dq}{dt} = -Bq|q| + \Delta P \quad (22)$$

relating the acceleration of flow to the pressure drop, ΔP , across the valve and the inertial effects of blood. L is the inertia of blood in the valve and coefficient B is the Bernoulli term which relates the kinetic energy of blood passing through the valve to the flow rate squared. This equation neglects viscous effects. L and B depend on instantaneous effective area of the valve A , which varies smoothly between minimum (closed valve), A_{closed} , and maximum (open valve), A_{open} , states according to function $\xi(t)$, representing the degree of the valve opening.

$$A = \xi A_{\text{open}} + (1 - \xi) A_{\text{closed}} \quad (23)$$

where ξ ranges between 0 and 1. The opening and closing of valves, $\xi(t)$, is modeled by the dynamic equation

$$\frac{d\xi}{dt} = \begin{cases} (1 - \xi)k_{\text{open}}\Delta P & \text{if } \Delta P > 0 \\ \xi k_{\text{close}}\Delta P & \text{if } \Delta P < 0 \end{cases} \quad (24)$$

where k_{open} and k_{close} are the rate constants of the valve opening and closing. We use this nonlinear valve model with respect to pressure in order to generate realistic hemodynamic measurements and flow waveforms through the valves that can be validated with echocardiogram data.

Additionally, before reaching the systemic circulatory system, we couple the left ventricle to a wave propagation model of the aorta, which accounts for time delays associated with reflected waves in the aorta. The significance of pulse wave amplification and early wave reflection in the understanding the pathophysiology of pathologies including hypertension has been shown in previous mathematical models and experimental studies [22, 23]. Therefore modeling wave propagation in the aorta provides a more realistic representation of the afterload on the LV. The model is based on linearized Euler equations for the conservation of mass and momentum for flow through the aorta. The equations are first solved numerically for a sudden impulse of incoming flow. During simulation of cardiac cycles, aortic pressures and flows from the reflected wave are solved by convolving the incoming wave form with the impulse response function. Details of the pulse wave propagation model of the aorta are described in Moulton and Secomb 2023 [16].

Finally, the spatially resolved models of the LV, RV, spherical atria, and aorta are coupled to a closed-circulation, lumped parameter model for the systemic and pulmonary arterial and venous systems represented by a set of 20 ordinary differential equations. Model components are summarized in Figure 5. All relevant and updated parameters are recorded in Table 2. A full list of parameter values used can be found in Moulton and Secomb 2023 [16]. Passive elastic parameters and baseline RV contractility were chosen to match normal PV loops in human studies [24].

Table 2: Updated parameters and constants from Moulton and Secomb 2023 [16]

Parameter	Symbol	Value
LV midwall	μ_{mid0}	0.55
Inner and outer angle that midwall splits forming RV	ϕ_s	$7\pi/12$
Stretch of reference state RV free wall	a_{40}	45
Stretch of reference state septum	a_{50}	0
LV passive elastic parameters	b_{ff}, b_{fx}, b_{xx}	20, 4.2, 12.8
LV strain energy function coefficient (kPa)	C_{LV}	0.3
RV passive elastic parameters	$b_{ffRV}, b_{fxRV}, b_{xxRV}$	10, 1, 3
RV strain energy function coefficient (kPa)	C_{RV}	0.2
Maximum LV contractile force generation (kPa)	k_{mLV}	200
LV force-velocity relationship (kPa·s)	k_{vLV}	67
Maximum RV contractile force generation (kPa)	k_{mRV}	200
RV force-velocity relationship (kPa·s)	k_{vRV}	67
Baseline pulmonary resistance (kPa·s/cm ³)	R_{pa}, R_{pp}, R_{pv}	0.0067, 0.008, 0.006

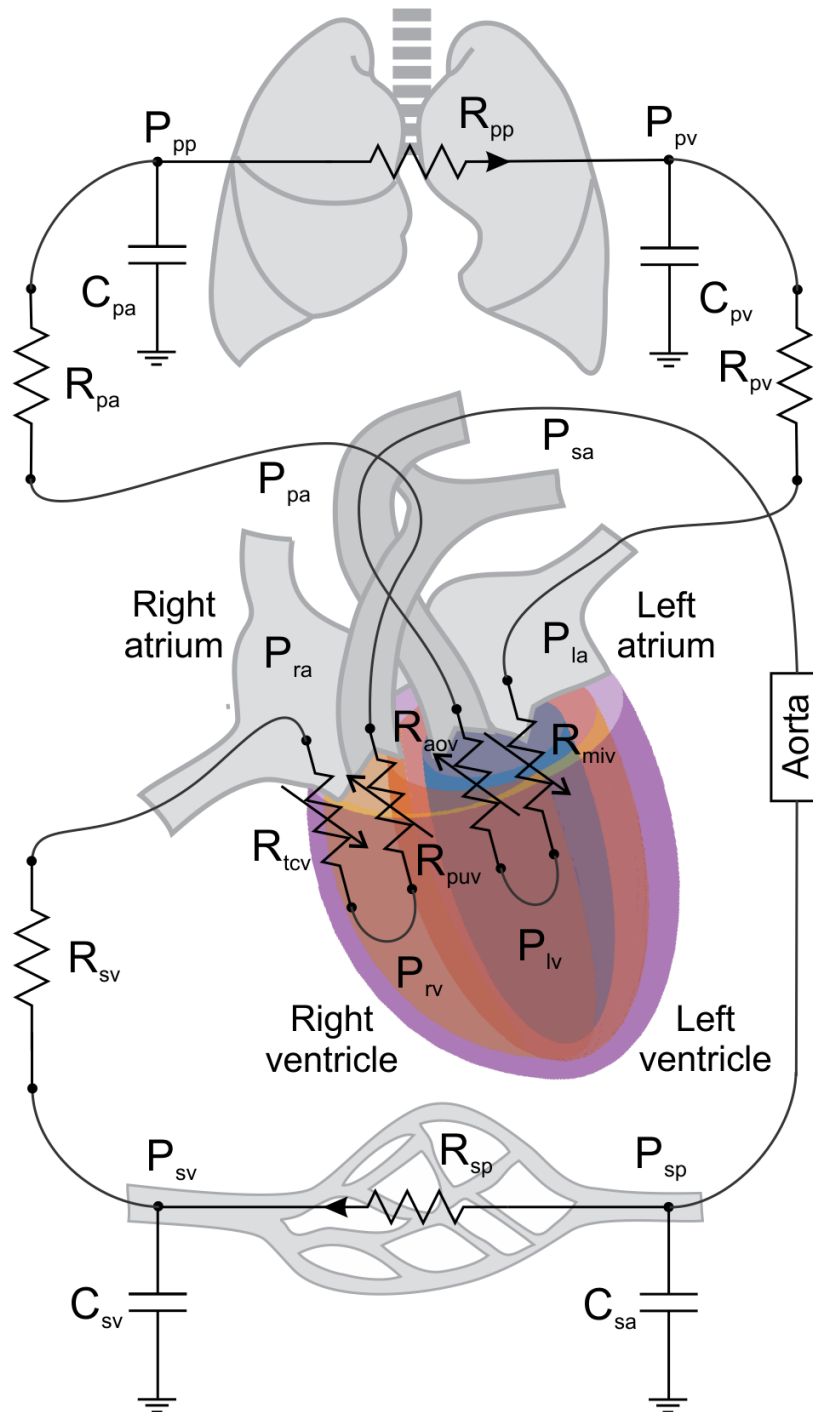


Figure 5: Schematic of circulatory system model depicted as an electrical circuit.

The four heart chambers are represented by spatially-resolved chambers with explicit representation of myocardial properties. Valve models have variable inertial effects with respect to flow represented by R_{tcv} , R_{puv} , R_{miv} , R_{aor} for each corresponding heart valve. The aorta is represented by a 1D wave propagation model. Other segments making up the pulmonary and systemic circulation are represented by lumped resistances and compliances including systemic peripheral R_{sp} and venous R_{sv} resistance, pulmonary arterial R_{pa} , peripheral R_{pp} and venous R_{pv} resistance, systemic arterial C_{sa} and venous compliance, and pulmonary arterial C_{pa} and C_{sa} compliance.

4 Results

4.1 Normal cardiac function

Simulations were run for 20 cardiac cycles when stroke volumes of RV and LV are close to equilibration. Figure 6 shows short and long axis view of computed LV and RV shapes including interventricular interaction.

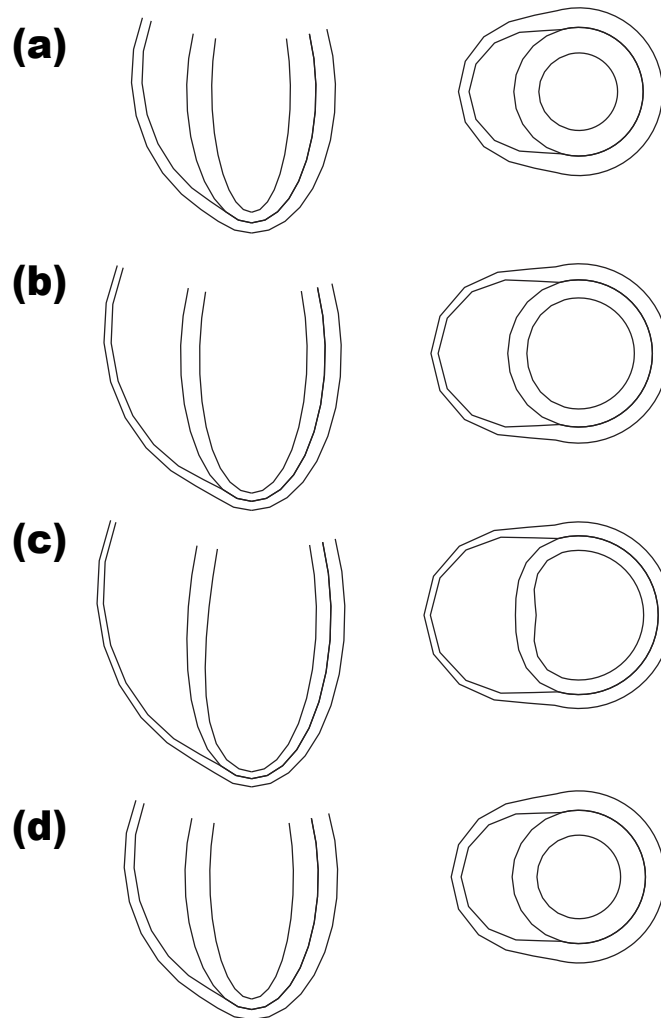


Figure 6: Long-axis (left column) and short-axis (right column) views of LV and RV wall deformations during the cardiac cycle.

(a) End systole (b) Mid diastole (c) End diastole (d) Mid systole

Figure 7 shows pressure-volume loops for normal values of all parameters, including effects of interventricular interaction. Pressures are typical for normal cardiac function with maximum systolic pressures of 130 mmHg in the LV and 30 mmHg in the RV. Stroke

volume is 76 mL. Corresponding time variations of pressures are shown in Figure 8 and flows shown in Figure 9. Using the zero-dimensional Bernoulli-type valve model captures E and A wave patterns characteristic of mitral inflow. Results are shown for the last 3 cycles.

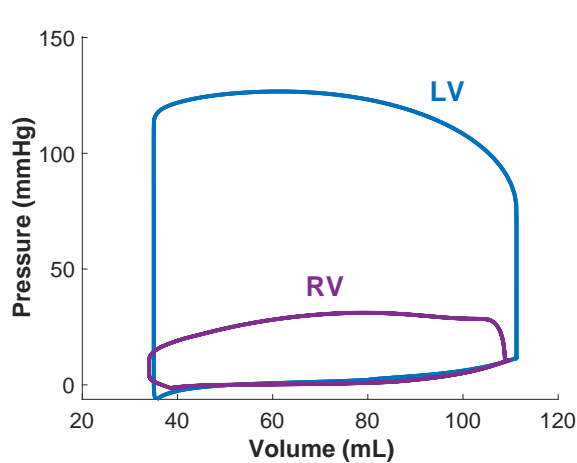


Figure 7: Normal pressure-volume loops: LV (blue) and RV (purple).

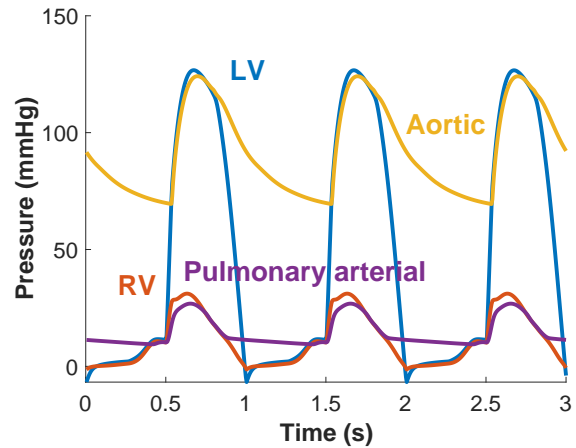


Figure 8: Normal pressures: LV (blue), RV (orange), aorta (yellow), and pulmonary arteries (purple).

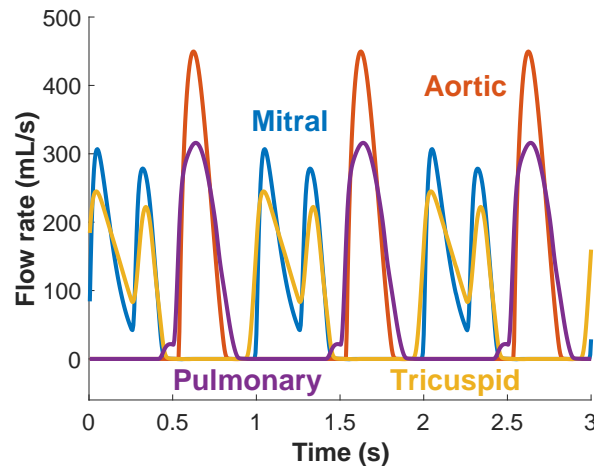


Figure 9: Normal flow rates through the tricuspid (yellow), pulmonary (purple), mitral (blue), and aortic (orange) valves.

4.2 Cardiac function with pulmonary hypertension

Pulmonary hypertension was simulated by increasing pulmonary resistance, including arterial (R_{pa}), venous (R_{pv}), and peripheral (R_{pp}) components, by factors one to five times. The model failed to reach equilibrium if pulmonary resistance acutely increased

without compensation by increased force generation in the RV. The effects of RV hypertrophy are represented by increasing RV force contractility (k_{mRV}, k_{vRV}) in proportion to the increase in pulmonary resistance.

The resulting changes in pressure-volume loops are shown in Figures 10 and 11. In the left ventricle, both systolic pressure and stroke volume are substantially decreased. Stroke volume decreased from 76 mL to 53 mL. LV systolic pressure decreased from 127 mmHg to 98 mmHg with the increase in pulmonary resistance and RV contractile force. RV systolic pressure increased from 31 mmHg to 78 mmHg. In the right ventricle, systolic pressure increased more than two times greater than baseline, from 31 mmHg to 78 mmHg. Flow rate decreased in every compartment, and in particular, mitral valve inflow showed an increase in E/A ratio from 1.07 to 1.5 in pulmonary hypertension (Figure 12).

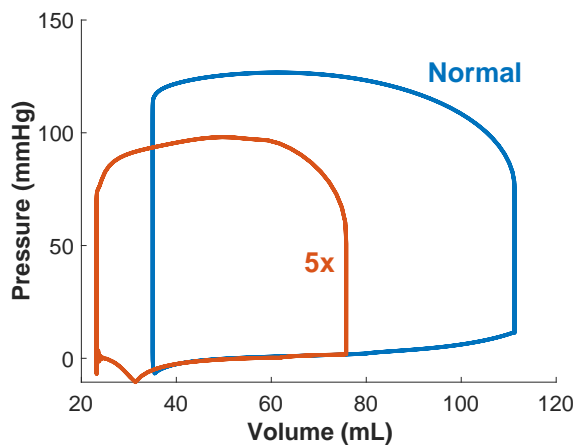


Figure 10: LV PV loops: Normal (blue); Five times (5x, orange) pulmonary resistance and RV contractility.

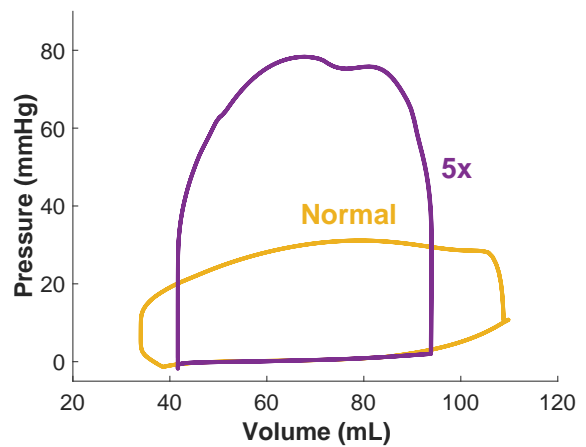


Figure 11: RV PV loops: Normal (yellow); Five times (5x, purple) pulmonary resistance and RV contractility.

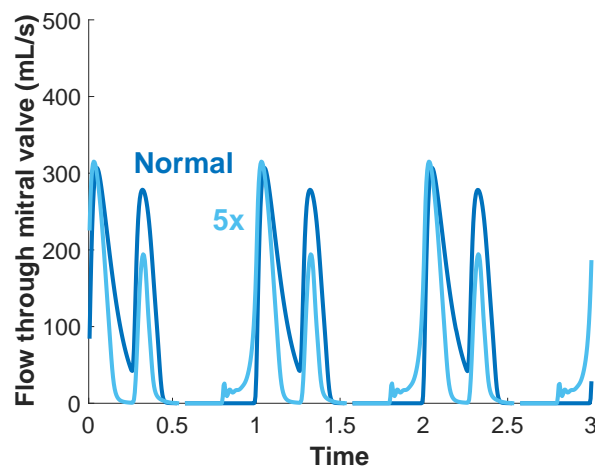


Figure 12: Mitral valve flow rate: Normal (dark blue); Five times (5x, light blue) pulmonary resistance and contractility.

4.3 Effects of interventricular interaction

To examine the effects of interventricular interactions, corresponding simulations were carried out without allowing for septal displacement by setting $a_5 = 0$. Figure 13 shows predicted LV and RV shapes in end diastole with (left) and without (right) septal displacement. Septal shift enlarges the RV cavity and reduces the LV cavity. Increases

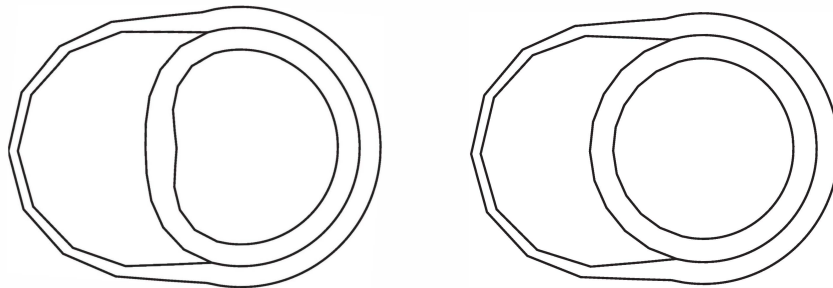


Figure 13: Short-axis view of LV and RV showing septal displacement when interventricular interactions are included (left) and no shift when excluded (right).

to pulmonary resistance resulted in decreases to stroke volume, despite inclusion of increase RV force generation to represent the effects of hypertrophy (Figure 14). Similar trends were seen with and without interventricular interactions. The stroke volume effects of interactions between the ventricles decreased with increasing levels of pulmonary hypertension.

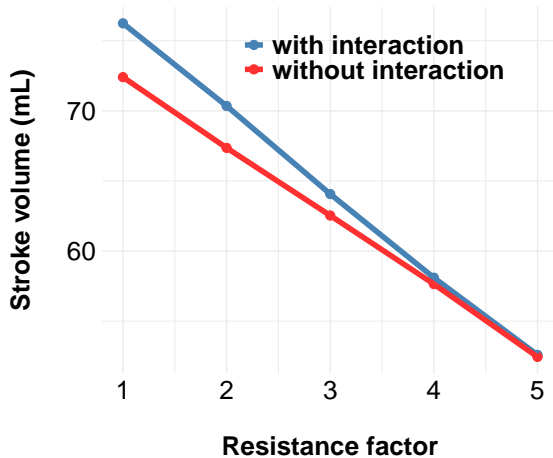


Figure 14: Decrease in LV stroke volume in response to increased pulmonary resistance and RV contractility.

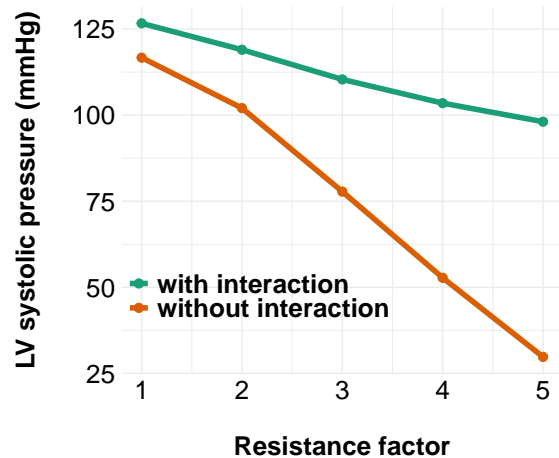


Figure 15: Decrease in LV systolic pressure in response to increased pulmonary resistance and RV contractility.

Figure 15 shows the effects of pulmonary hypertension on systolic pressure in the LV and RV with and without interventricular interactions. RV systolic pressure increases with pulmonary hypertension, as previous discussed (Figure 11). The increase in RV pressure

is similar with and without septal shift. Left ventricular pressure decreased (up to 22%) with an increase in pulmonary resistance and RV contractility, however the decrease in pressure is greater (up to 74%) when interventricular interactions are excluded.

5 Discussion

In this work, we have developed a computationally fast, spatially resolved model of the right and left ventricle that can predict the effects of interventricular interaction on deformations of the ventricles. We describe the biventricular motion of the heart with a small number of degrees of freedom using a volume-preserving mapping and five time-dependent parameters. By spatially resolving both the right and left ventricle, we are able to capture the direct mechanical interaction of the ventricles via shift of the interventricular septum. The presented model serves as an intermediate between lumped parameter approaches such as the varying elastance model, which groups all geometrical features of the ventricles in a single volume change term and finite element methods with high spatial resolution, requiring thousands of degrees of freedom for similar fidelity. In effect, the model captures an explicit description of the LV and RV geometry and its main modes of deformations including base-to-apex, circumferential, and torsional deformations, over multiple cardiac cycles at a low computational cost. Model solutions are obtained in minutes to seconds compared to hours making it suitable for routine clinical use. Model outputs including pressures, volumes, ventricle dimensions, flows, valve flow velocity are comparable to data collected by echocardiography.

We apply the model to investigate the effects of interventricular interactions on pulmonary arterial hypertension (PAH). We simulated PAH by increasing pulmonary resistance and found that the model failed to equilibrate, suggesting that the heart cannot respond well to sudden increases in pulmonary resistance without adaptation. This finding is consistent with clinical observations as for the case of patients with pulmonary embolism, where increase in RV afterload can result in acute RV failure. RV adaptation and hypertrophy are necessary for the heart to sustain function in the context of PAH. Therefore, we represented the effects of hypertrophy of the right ventricle by increasing force of RV contraction proportional to increases in pulmonary resistance. Although the model allows for deformations in RV cavity size, RV wall adaptations and hypertrophy is currently not modeled in our geometrical framework. PAH is defined as an RV systolic pressure of above 40 mmHg [25], and we were able to simulate an increase of RV systolic pressure from 31 mmHg to 78 mmHg by increasing pulmonary resistance and contractility up to five times greater (Figure 11). We found that PAH leads to significant rises in pulmonary artery pressure, but reductions systemic arterial pressure and stroke volume, despite proportionally increasing RV contractility (Figures 10, 11). Left shift of the LV PV loop indicates impaired LV diastolic filling. This may be explained by reduced LV preload due to pulmonary edema secondary to PAH [26].

To test for the effects of interventricular interactions, we ran simulations of PAH while allowing and restricting septal displacement. We found that including interventricular in-

teractions resulted in higher stroke volume at baseline and small increases in pulmonary resistance and RV contractility. Stroke volume also decreases at a faster rate with interventricular interactions. However, septal displacement has little effect on LV stroke volume when pulmonary resistance and RV contractility elevates substantially up to 5 times greater (Figure 14). We propose that increased RV contractility may be compensating for reduced LV diastolic filling, resulting in similar stroke volume with and without septal shift. As shown in Figure 15, inclusion of interventricular interactions reduced the percent decrease in LV pressure from 74% without septal shift to only 22% with displacement. This finding suggests that septal displacement facilitates the highly contractile RV to help maintain LV systolic pressure under conditions of reduced LV preload from PAH.

Our results contradict the common hypothesis that ventricular dependence mediated via septal shift plays an adverse role by impairing filling of the LV [27, 10, 25]. For instance, an MR imaging study of patients with severe PAH correlated septal shift with decreased LV filling rate and LV end-diastolic volume, then suggested septal displacement interferes with LV filling contributing to decreased stroke volume [10]. Although our model supports that increased pulmonary resistance decreases stroke volume (Figure 10, 11), our experiment restricting septal displacement shown in Figure 14 suggests that direct interventricular interaction does not further stroke volume reduction. In fact, our model proposes that septal shift may contribute positively to the regulation of LV systolic pressure in PAH. These effects are dependent on the presence of RV hypertrophy and increased contractility. We also found mitral valve flow showed an increase in E/A ratio from 1.07 to 1.5 in pulmonary hypertension. Relative increases in E/A ratio may indicate elevated LV compliance, however, 1.5 is still within the normal range [28]. Additionally, clinical studies have shown that PAH decreases E/A ratio [27].

Limitations to the model include: RV hypertrophy cannot be represented geometrically from our assumed axisymmetric LV initial configuration. Currently, the model allows for deformations in RV cavity by displacement of the RV free wall and septum. To also enable adaptation and hypertrophy of the RV independent of the LV free wall requires a non-axisymmetric initial configuration, where outer wall parameter μ_{out0} can change as a function of azimuthal angle ϕ_0 . The present model can only increase the thickness of the RV wall by also increasing the LV wall thickness. Thus, the effect of RV hypertrophy is represented by an increase in RV force of contraction, k_{mRV}, k_{vRV} , which is not dependent on myocardial thickness or RV stresses and strains. We also did not increase passive stiffness, C_{RV} , with hypertrophy and including this effect would likely result in steeper diastolic filling curves in PAH compared to normal (Figures 10, 11).

In the biventricular model, we consider 3 types of interventricular interactions: (1) displacement of the septum, (2) stretching of the RV free wall from LV motion, and (3) indirect effects of volume shifts between the systemic and pulmonary circulation. Our simulations excluding interventricular interactions only restricted septal shift, and allowed the other forms of interaction. Although we only examine the role of the septum in this study, the proposed model is suitable for investigating these other aspects of ventricular dependence or exploring its role in other cardiomyopathies.

6 References

- [1] I. Starr, W.A. Jeffers, and R.H. Meade. “The absence of conspicuous increments of venous pressure after severe damage to the right ventricle of the dog, with a discussion of the relation between clinical congestive failure and heart disease”. In: *American Heart Journal* 26.3 (1943), pp. 291–301. DOI: 10.1016/S0002-8703(43)90325-4.
- [2] A.A. Bove and W.P. Santamore. “Ventricular interdependence”. In: *Progress in cardiovascular diseases* 23.5 (1981), pp. 365–388. DOI: 10.1016/0033-0620(81)90022-0.
- [3] S. J. Dong, E. R. Smith, and J. V. Tyberg. “Changes in the radius of curvature of the ventricular septum at end diastole during pulmonary arterial and aortic constrictions in the dog”. In: *Circulation* 86.4 (1992), pp. 1280–1290. DOI: 10.1161/01.cir.86.4.1280.
- [4] F. Jardin et al. “Quantitative two-dimensional echocardiography in massive pulmonary embolism: emphasis on ventricular interdependence and leftward septal displacement”. In: *Journal of the American College of Cardiology* 10.6 (1987), pp. 1201–1206. DOI: 10.1016/s0735-1097(87)80119-5.
- [5] B. B. Stojnic et al. “Left ventricular filling characteristics in pulmonary hypertension: a new mode of ventricular interaction”. In: *British heart journal* 68.1 (1992), pp. 16–20. DOI: 10.1136/hrt.68.7.16.
- [6] S. Ghio et al. “Independent and additive prognostic value of right ventricular systolic function and pulmonary artery pressure in patients with chronic heart failure”. In: *Journal of the American College of Cardiology* 37.1 (2001), pp. 183–188. DOI: 10.1016/s0735-1097(00)01102-5.
- [7] S. Aschauer et al. “The right heart in heart failure with preserved ejection fraction: insights from cardiac magnetic resonance imaging and invasive haemodynamics”. In: *European journal of heart failure* 18.1 (2016), pp. 71–80. DOI: 10.1002/ejhf.418.
- [8] S.J. Dong et al. “Regional left ventricular systolic function in relation to the cavity geometry in patients with chronic right ventricular pressure overload. A three-dimensional tagged magnetic resonance imaging study.” In: *Circulation* 91.9 (1995), pp. 2359–2370. DOI: 10.1161/01.cir.91.9.2359.
- [9] J. T. Marcus et al. “Impaired left ventricular filling due to right ventricular pressure overload in primary pulmonary hypertension: noninvasive monitoring using MRI”. In: *Chest* 119.6 (2001), pp. 1761–1765. DOI: 10.1378/chest.119.6.1761.
- [10] C. Tji-Joong Gan et al. “Impaired left ventricular filling due to right-to-left ventricular interaction in patients with pulmonary arterial hypertension”. In: *American Journal of Physiology-Heart and Circulatory Physiology* 290.4 (2006), H1528–H1533. DOI: 10.1152/ajpheart.01031.2005.

- [11] L. Garber, S. Khodaei, and Z. Keshavarz-Motamed. “The Critical Role of Lumped Parameter Models in Patient-Specific Cardiovascular Simulations”. In: *Arch Computat Methods Eng* 29 (2022), pp. 2977–3000. DOI: 10.1007/s11831-021-09685-5.
- [12] B. W. Smith et al. “Minimal haemodynamic system model including ventricular interaction and valve dynamics”. In: *Medical Engineering Physics* 26.2 (2004), pp. 131–139. ISSN: 1350-4533. DOI: 10.1016/j.medengphy.2003.10.001.
- [13] S. Land et al. “Verification of cardiac mechanics software: benchmark problems and solutions for testing active and passive material behaviour”. In: *Proceedings of the Royal Society A: Mathematical, Physical and Engineering Sciences* 471.2184 (2015), p. 20150641. DOI: 10.1098/rspa.2015.0641.
- [14] J. Lumens et al. “Three-wall segment (TriSeg) model describing mechanics and hemodynamics of ventricular interaction.” In: *Ann Biomed Eng.* 37.11 (2009), pp. 2234–2235. DOI: 10.1007/s10439-009-9774-2.
- [15] S.M. Kim et al. “Computational modeling of ventricular-ventricular interactions suggest a role in clinical conditions involving heart failure.” In: *Front. Physiol.* 14 (2023), p. 1231688. DOI: 10.3389/fphys.2023.1231688.
- [16] M.J. Moulton and T.W. Secomb. “A fast computational model for circulatory dynamics: effects of left ventricle-aorta coupling”. In: *Biomechanics and modeling in mechanobiology* 22.3 (2023), pp. 947–959. DOI: 10.1007/s10237-023-01690-w.
- [17] B. D. Hong, M. J. Moulton, and T. W. Secomb. “Simulation of Left Ventricular Dynamics Using a Low-Order Mathematical Model”. In: *Cardiovascular Engineering and Technology* 8.4 (2017), pp. 480–494. DOI: 10.1007/s13239-017-0327-9.
- [18] B. D. Hong, M. J. Moulton, and T. W. Secomb. “Modeling left ventricular dynamics with characteristic deformation modes”. In: *Biomechanics and modeling in mechanobiology* 18.6 (2019), pp. 1683–1696. DOI: 10.1007/s10237-019-01168-8.
- [19] M.J. Moulton and T.W. Secomb. “A Low-Order Parametric Description of Left Ventricular Kinematics”. In: *Cardiovascular Engineering and Technology* 5.4 (2014), pp. 348–358. DOI: 10.1007/s13239-014-0191-9.
- [20] J.P. Mynard et al. “A simple, versatile valve model for use in lumped parameter and one-dimensional cardiovascular models.” In: *Int. J. Numer. Meth. Biomed. Engng.* 28 (2012), pp. 626–641. DOI: 10.1002/cnm.1466.
- [21] T. Arts et al. “Adaptation to mechanical load determines shape and properties of heart and circulation: the CircAdapt model”. In: *American Journal of Physiology-Heart and Circulatory Physiology* 288.4 (2005), H1943–H1954. DOI: 10.1152/ajpheart.00444.2004.
- [22] P. Segers and P. Verdonck. “Role of tapering in aortic wave reflection: hydraulic and mathematical model study”. In: *Journal of Biomechanics* 33.3 (2000), pp. 299–306. ISSN: 0021-9290. DOI: 10.1016/S0021-9290(99)00180-3.
- [23] W.R. Milnor. “Arterial impedance as ventricular afterload”. In: *Circulation Research* 36.5 (1975), pp. 565–570. DOI: 10.1161/01.RES.36.5.565.

- [24] W.K. Cornwell et al. “New Insights into Right Ventricular Function among Patients with Left Ventricular Assist Devices Using High Fidelity Conductance Catheters to Generate Real Time Pressure Volume Loops”. In: *The Journal of Heart and Lung Transplantation* 38.4 (2019), S19–S20. ISSN: 1053-2498. DOI: 10.1016/j.healun.2019.01.031.
- [25] S. Dellegrottaglie et al. “Pulmonary hypertension: accuracy of detection with left ventricular septal-to-free wall curvature ratio measured at cardiac MR”. In: *Radiology* 243.1 (2007), pp. 63–69. DOI: 10.1148/radiol.2431060067.
- [26] S. Breitling et al. “The pathophysiology of pulmonary hypertension in left heart disease”. In: *American Journal of Physiology-Lung Cellular and Molecular Physiology* 309.9 (2015), pp. L924–L941. DOI: 10.1152/ajplung.00146.2015.
- [27] M. Kasner et al. “Left ventricular dysfunction induced by nonsevere idiopathic pulmonary arterial hypertension: a pressure-volume relationship study”. In: *American journal of respiratory and critical care medicine* 186.2 (2012), pp. 181–189. DOI: 10.1164/rccm.201110-18600C.
- [28] P.M. Mottram and T.H. Marwick. “Assessment of diastolic function: what the general cardiologist needs to know.” In: *Heart*. 91.5 (2005), pp. 681–695. DOI: 10.1136/hrt.2003.029413.